INFLUENCE OF CROSS-SECTIONAL SHAPE ON FLOW PATTERNS IN AN OPEN-CHANNEL CONFLUENCE

LAURENT SCHINDFESSEL[1], STÉPHAN CREËLLE[1] & TOM DE MULDER[1]

[1] *Hydraulics Laboratory, Dep. of Civil Engineering, Ghent University, Ghent, Belgium,*
laurent.schindfessel@ugent.be

ABSTRACT

The state-of-the-art hydrodynamic knowledge on schematized open-channel confluences is largely based on laboratory experiments in channels with a rectangular cross-section. Since in practice man-made canals often have a non-rectangular cross-section, the question can be raised to which extent the knowledge on open-channel confluences still holds for confluences of that type of canals. Therefore, this paper examines the influence of three cross-sectional shapes on the flow patterns in an asymmetric 90° open-channel confluence with fixed concordant bed and subcritical flows throughout. Large-eddy simulations are performed for a rectangular, a chamfered rectangular and a trapezoidal section. The simulations for the non-rectangular sections show that the location of both the mixing layer between the incoming flows and the shear layer between the separation zone and the contracted section are altered in comparison to the rectangular section case. Also the evolution of the separation zone is found to be different. It is demonstrated that the distribution of incoming momentum and the shape of the confluence corners are primary causes of the observed deviations.

Keywords: open channel confluence, cross-section, trapezoidal, large-eddy simulation

1. INTRODUCTION

Open channel confluences are ubiquitous in networks of rivers and manmade canals. They exist in a multitude of forms and many parameters are known to influence the flow patterns associated to (fixed bed) confluences. Geometrical parameter are e.g. the junction angle, the shape of the incoming channels (both in lay-out as in cross-sectional shape), the possible bed discordance, the ratio of channel widths, the bed roughness, etc. Hydraulic parameters are e.g. the ratio of the incoming discharges, the Froude numbers in the channels, etc. For a number of parameters, a systematic study of their effect on the hydrodynamics in (schematized) confluences has been already reported in literature. To the best of our knowledge, this has not yet been the case for the cross-sectional shape. Therefore, the present paper wants to contribute to revealing the influence of this parameter. More specifically, attention will be focused on asymmetrical 90° confluences with fixed and concordant bed, subjected to subcritical flow throughout. Figure 1 presents a conceptual model of such an open-channel confluence, showing the main flow features: flow stagnation, flow separation, flow contraction and an intense mixing layer (Rice et al. 2008). It is in this configuration that the influence of the cross-sectional shape will be studied.

For straight open channels, it is known that secondary currents might be present. These secondary currents are in magnitude small compared to the main flow (Tominaga et al., 1989), yet are known to have substantial influence on the patterns of streamwise velocity, turbulent flow properties and sediment transport (Nezu et al., 1989; Blanckaert et al., 2010). The patterns of secondary currents are affected by the aspect ratio of the channel, the roughness of bottom and walls, and the shape of the cross-section (see e.g. Tominaga et al., 1989; Blanckaert et al., 2010). Especially the influence of cross-sectional shape is relevant for this research. Tominaga et al. (1989) compare, amongst other things, secondary structures in a rectangular and a trapezoidal cross-section (by means of experiment and simulation). They find that in a trapezoidal channel, there are three instead of two secondary currents near the bank, and that the velocity dip phenomenon does not appear. The experiments of Blanckaert et al. (2010) confirm these results, and elaborate on the influence of roughness on trapezoidal channels.
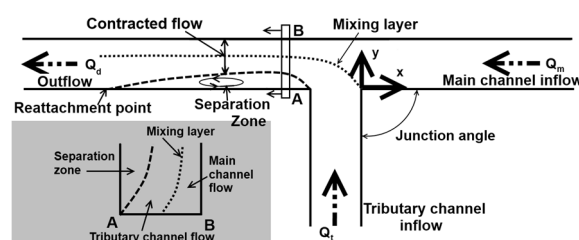

Figure 1. Conceptual model of an open-channel confluence, indicating the main flow features.

The demonstrated influence of the cross-sectional shape in a straight channel already indicates that this parameter might be influential in a confluence as well. In particular, depending on the cross-sectional shape, the incoming channels of the confluence will have a different fully developed velocity profile, which might result in different mixing of these two streams. Additionally, the shape of the confluence area itself might influence the extent of flow features like the contraction and the separation zone.

Yet, most laboratory experiments (for asymmetrical, subcritical open channel confluences with schematized cross-sections and non-movable, concordant bed, an overview of which has been presented in table 1 of Schindfessel et al (2014)), have been conducted with rectangular cross-sections. A notable exception is Anwar (1955), who worked with trapezoidal channels of different width. Although his study is pioneering in the sense that he covers all aspects of a confluence from an engineer's point of view, the limitations of the measurement techniques at that time only allowed measurements of water heights and a limited number of longitudinal velocities.

In contrast to the laboratory experiments, many man-made canals (e.g. for purposes of navigation, irrigation, drainage etc.) adopt a non-rectangular cross-section. Rectangular sections made with in situ cast concrete e.g., commonly are chamfered to simplify the removal of the formwork. Manmade canals excavated in loose soil, usually have sloped banks, hence a trapezoidal cross-section. Therefore, the research question of this study is to what extent the existing knowledge acquired in rectangular sections can be transferred to confluences in which the channels have other cross-sectional shapes.

This paper thus aims at pointing out the differences in confluence flow patterns when the cross-sectional shape of the channels changes. To this end, large-eddy simulations (LES) are performed, as these allow to solve complex flow problems such as bends (e.g. van Balen et al., 2009) and confluences (e.g. Constantinescu et al., 2012) relatively accurately and, moreover, provide sufficient resolution for a thorough comparison. Three types of cross-section will be considered in this paper: a pure rectangular section, a chamfered rectangular section and a trapezoidal section (figure 2).

In section 2 of this paper, laboratory experiments are presented that will be used in section 3 to validate the LES of a confluence with chamfered cross-sections. Section 3 also describes the set up and verification of the numerical model. Two other versions of the numerical model will then be made, in which only the geometry of the chamfered cross-sections will be changed, to a pure rectangular and a trapezoidal section respectively. In section 4, the numerical results for the three cross-sectional shapes will be presented and the differences will be discussed. Conclusions are presented in section 5.

2.   LABORATORY EXPERIMENTS

The experiments that are used here to validate the numerical model, were described in Schindfessel et al. (2014). They consist of measurements in a concrete 90° confluence, with a chamfered cross-section. The corresponding hydraulic parameters are a Froude number of 0.05, a Reynolds number based on the hydraulic radius of 98 000, and the discharge ratio q, defined as (figure 1):

$$q = \frac{Q_m}{Q_d} = \frac{Q_m}{Q_m + Q_t} \qquad [1]$$

assuming a value of 0.25 or 0.05. For the present study, only the results of the experiment with q = 0.25 are used.

Velocity fields were measured by means of an ADV in a number of cross-sections in the confluence flume. Besides one cross-section sufficiently upstream of the confluence in each of the incoming channels, detailed measurements were also carried out in two cross-sections within the confluence area. The latter cross-sections are situated at $x = -1.33W_d$ and $x = -2W_d$ (making use of the coordinate system defined in figure 2). Additionally, the surface velocities were measured by means of LSSPIV.
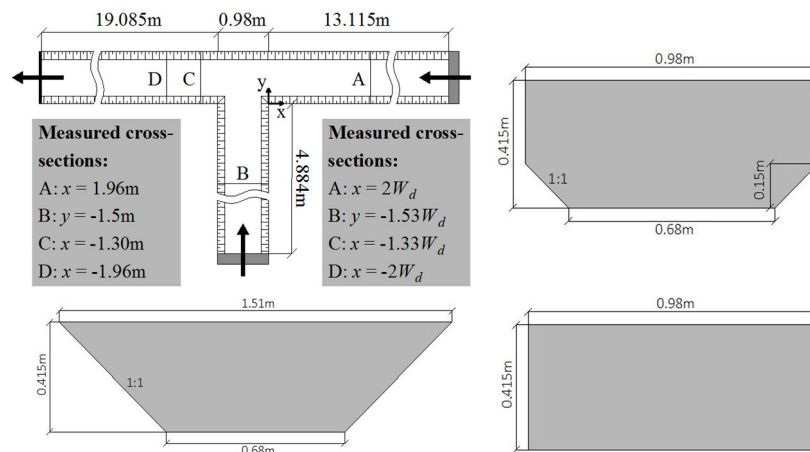

Figure 2. Plan view of the laboratory flume (upper left panel, indicating the position of the ADV measurements) with chamfered cross-sections (upper right panel). Rectangular cross-section (lower right panel) and trapezoidal cross-section (lower left panel) that will also be investigated in the numerical simulations.

The details of the measuring techniques were presented in Schindfessel et al. (2014), hence only the main characteristics will be repeated here. The ADV measurements were taken at a frequency of 30Hz, during an interval of 2 min. They were despiked according to the algorithm of Goring & Nikora (2002), discussed by Wahl (2003). Only measurements with a sufficiently high signal-to-noise ratio and a correlation higher than 80% were retained. The total measurement error of ADV was estimated by measuring in a certain point after the discharge was set and the measuring device was positioned. This resulted in a standard deviation on the two-minute mean velocity of (0.0009, 0.0016, 0.0018) m/s. Since this point was located in a straight incoming channel, the standard deviation does not account for the presence of steep gradients, which will induce extra errors. Due to the complex flow patterns in a confluence, many local gradients exist and it is therefore hard to characterize the measurement error by one single number. Consequently, the aforementioned standard errors should be treated with care. The LSSPIV measurements were compared with the ADV profiles close to the surface (at cross-sections $x = -1.33W_d$ and $x = -2W_d$), and a good agreement was found.

The coordinate system used in this paper is introduced in figure 2. Note that the z-axis points upwards, establishing a right-handed system. Velocity components in the x, y and z direction are denoted as u, v and w respectively. A bar, e.g. $\bar{u}$, indicates time-averaged values.

3. NUMERICAL SIMULATION

3.1 The different cross-sectional shapes

The chamfered cross-section that is used for the lab experiments, is the benchmark case for the numerical simulations. In order to enable a fair comparison with the cases of the other cross-sectional shapes that will be simulated in this paper, the latter cases should be defined carefully. To this end, two principles will be adopted.

First, the Froude number, which is the dominant dimensionless parameter for open channel flow, will be kept constant for the three cases. More specifically, the Froude number will be taken equal to the experimental value of 0.05 for each simulated cross-sectional shape. Note that this low Froude number is representative for lowland rivers (Khublaryan 2009). The Froude number for a non-rectangular section is defined as:

$$Fr_d = \frac{U_d}{\sqrt{gA_d/W_d}} \qquad [2]$$

In which U is the cross-sectionally averaged velocity ($\mathrm{ms^{-1}}$), g the gravitational acceleration ($9.81\,\mathrm{ms^{-2}}$), A the cross-sectional area ($\mathrm{m^2}$) and W the width at the surface (m). Here, the parameters of the channel downstream of the confluence are to be used, indicated by the subscript d, since the aforementioned value of 0.05 is defined accordingly.

Secondly, the (downstream) water depth h_d is taken equal for all cross-sectional shapes. Equal water depths h are preferred over equal depth-to-width ratios, because a small difference in water depth is considered more influential than a small difference in depth-to-width ratio.

With the aforementioned principles, a rectangular and trapezoidal cross-sectional shape are derived from the lab experiment with the chamfered cross-section. The resulting cross-sections are depicted in figure 2 and the corresponding parameters are summarized in Table 1.

Table 1. Parameters of the different cross-sectional shapes. Note that W_d represents the channel width at the surface.

	RECTANGULAR SECTION	CHAMPFERED SECTION	TRAPEZOIDAL SECTION
$A_d\ [m^2]$	0.407	0.384	0.454
$U_d\ [m/s]$	0.107	0.104	0.091
$W_d\ [m]$	0.98	0.98	1.51
$h\ [m]$	0.415	0.415	0.415
$Fr\ [\text{-}]$	0.053	0.053	0.053

3.2 Set-up of Large-Eddy Simulations

The large-eddy simulations (LES) were performed in the OpenFOAM suite, which is an open-source code for computational fluid dynamics. The equations that were solved, namely the filtered Navier-Stokes equations, will not be stated here, as there are ample textbooks on LES that provide an in-depth discussion (e.g. Sagaut 2006). As a subgrid-scale model, the standard Smagorinksy model was chosen, with a parameter setting of $C_s = 0.167$. Time and space discretization were second order accurate.

Although the highest precision in LES can be achieved when the boundary layers are fully resolved, this poses two specific problems for the field of hydraulics. First, fully resolving the boundary layer requires increasing computation power for increasing Reynolds number. Hence, for high Reynolds number, such fine resolution is not feasible (Rodi et al. 2013). Secondly, if a relatively rough wall is to be simulated, as is often the case in hydraulics, complex solutions are necessary in a wall-resolved LES, see e.g. Stoesser (2014). Therefore, this study does not resolve the rough boundary layer, but makes use of a wall function. This reduces computational costs and allows to simulate rough boundaries. The law of the wall, which is the basic assumption of the wall function, might however not be valid in complex 3D flows, introducing additional approximations. Nevertheless, the use of wall functions has been successfully applied to complex flows (see e.g. van Balen et al. 2009 for the flow in a mildly curved river bend). Summarizing, the presented LES make use of a wall function, with a roughness parameter k_s equal to 2mm (representative for the concrete walls of the laboratory flume).

At the downstream boundary, a convective boundary condition was applied. At the incoming boundaries, turbulent inflow was mimicked by introducing random fluctuations on the mean velocity profiles, of which the amplitude was based on the experimentally measured fluctuations. The length of the incoming streams was taken sufficiently long so that these fluctuations can evolve to physical turbulence. The free surface was treated as a rigid lid, which is an acceptable approximation given the low Froude number of 0.05 and the limited water height differences that were measured experimentally.

Each branch in the numerical confluence had a length of 5m. For the incoming channels, this rather large length is chosen to ensure that the turbulent flow can become fully developed before the flow features typical for the confluence (like e.g. the stagnation zone) start to develop. For the downstream channel, the length was sufficient to characterize the mixing layer, although attaining a fully mixed downstream flow would require a multiple of the current length. After a sufficiently long simulation time, mean values were calculated over a time interval of 440s.

Each of the numerical models corresponding to a different cross-sectional shape had its distinct mesh. Table 2 shows how many cells were used in the transversal and vertical direction of a cross-section, as well as the total amount of cells. Changes in the number of cells are due to modeling the exact geometry of the cross-section, as the need for a smooth mesh sometimes required a slightly lower or higher number of cells. Nevertheless, the cells in the three models had comparable dimensions.

Table 2. Mesh parameters of the different cross-sectional shapes in the numerical model.

	RECTANGULAR SECTION	CHAMPFERED SECTION	TRAPEZOIDAL SECTION
# CELLS IN TRANSVERSAL DIRECTION	98	106	94
# CELLS IN VERTICAL DIRECTION	37	37	41
TOTAL # CELLS	$5.4 \; 10^6$	$4.2 \; 10^6$	$4.3 \; 10^6$

3.3 Verification of numerical simulations

A requirement for any numerical simulation is verifying whether the simulations are independent of the (artificial) boundaries and the mesh. Specifically for LES, an additional check should be made to make sure that a sufficient part of the turbulent kinetic energy is resolved on the mesh. Typically, 80% to 90% of the turbulent kinetic energy should be resolved (Rodi et al. 2013). To check this requirement, the methodology used in Coussement et al. (2012) was adopted.

The outlet boundary was sufficiently far away to have no influence on the domain of interest. For the wall model to be valid, the first cell should be located minimally 20 to 30 dimensionless wall units from the wall (Sagaut 2006; Rodi et al 2013). This is a general rule of thumb, as for a zone of zero velocity, such as the recirculation zone, the dimensionless wall distance cannot be defined. Nevertheless, the mesh was built so that the first cell was located according to the aforementioned criterion in zones of clear downstream flow. For zones of near-zero velocity (where the position of the first cell does not respect the aforementioned criterion) the OpenFOAM wall-function automatically switches off when the use of a wall function is not valid, reducing to the wall boundary for wall-resolved LES.

3.4 Validation of numerical simulations

The validation of the LES consists of comparing the numerical simulations of the chamfered section with the experimental measurements, which were discussed in section 2. The mean inlet profiles show good comparison with the experiments. For two sections that were measured with ADV, namely $x/W_d = -1.33$ and $x/W_d = -2$, figure 3(a) presents the validation of the results, while figure 3(b) compares with the LSSPIV data.

It follows from figure 3 that the two sections measured with ADV show a reasonable agreement with the numerical simulations in terms of the mean longitudinal velocity compenent $\bar{u}$. Points in the contracted section and the separation zone have a good agreement, while the points with the worst agreement are located in the shear layer next to and below the separation zone. This can be explained because a large velocity gradient is present in this shear layer, which magnifies differences. It should be mentioned that this region is the most challenging location both for the numerical simulations and the laboratory experiments. As will become clear in figures 9 and 10 of paragraph 4.4 the mean transversal and lateral velocities $\bar{v}$ and $\bar{w}$ are simulated in a less satisfactorily way. Although the general trends are present, the secondary cells in the contracted section do not appear that well in the present simulations.

Figures 3 and 4 show that the simulated surface velocities agree well with the LSSPIV experiments of LSSPIV. The width of the separation zone and the velocity distribution in the contracted section are well captured by the LES.

Note that paragraph 4.4 will also present some additional validation of the numerical simulations with a rectangular cross-section, based on experiments and simulations published in literature.
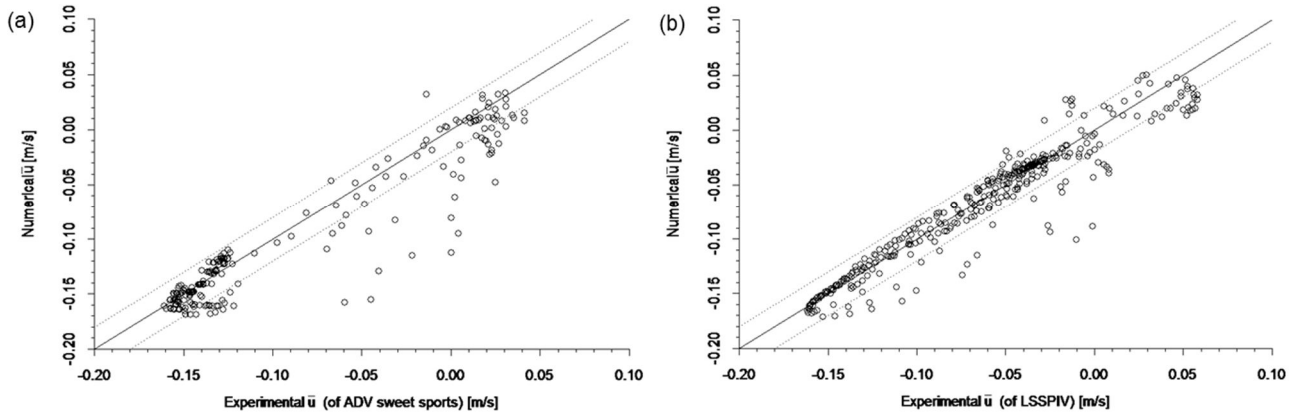
Figure 3. Validation of numerical data for mean longitudinal velocity $\bar{u}$ by comparison with the laboratory experiment.
Figure (a) comparison to experimental data (sweet spots) measured with ADV in the sections $x/W_d = -1.33$ and $x/W_d = -2$.
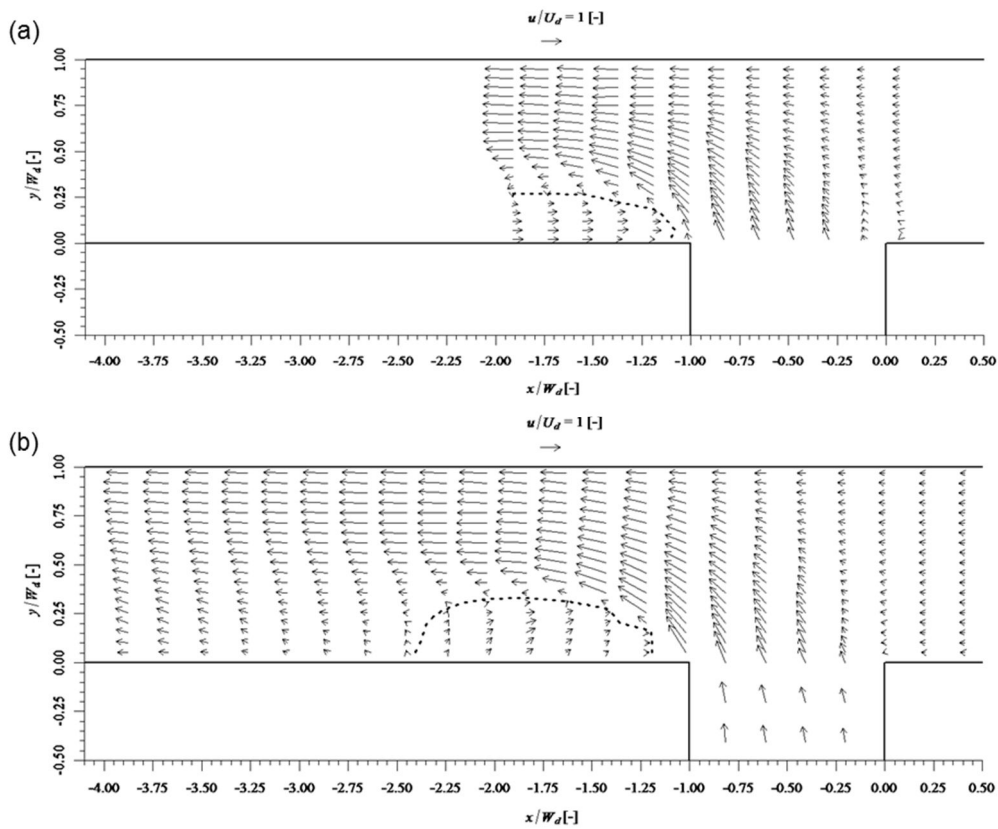Figure (b): comparison to LSSPIV data.

Figure 4. Validation of numerical results by comparison with the laboratory experiment.
Figure (a) LSSPIV data, figure (b): LES of chamfered cross-section. The dashed line presents $\bar{u} = 0$.

4. COMPARISON OF DIFFERENT CROSS-SECTIONS

This section will discuss the results of the numerical simulations, in a stepwise fashion. First, the incoming momentum will be shown, then the position of the mixing layer and the surface velocity. Finally, a selection of vertical planes is shown to elucidate the observed differences.

4.1 Inflow momentum

It is expected that the distribution of the inflow momentum, which differs for the different cross-sectional shapes, might have important effects on the mixing in the confluence. To characterize the incoming streamwise momentum, the vertical profiles of momentum averaged over the width are determined. Neglecting the constant fluid density, the streamwise momentum averaged over the width, m_s, is calculated as follows:

$$m_s(z) = \int_0^W \overline{u_s(y,z)^2} \, \mathrm{d}y \qquad [3]$$

5

where $\overline{u_s}$ indicates the mean streamwise velocity. In the main incoming channel, $\overline{u_s} = \overline{u}$, while in the tributary channel, $\overline{u_s} = \overline{v}$. If this parameter m_s has a large value, it indicates that a large streamwise momentum is present at this height. Because the wall roughness is known to alter the momentum distribution (Creëlle et al., 2014), all simulations have the same wall roughness. Differences in m_s are therefore only attributed to the cross-sectional shape. The m_s parameter is made dimensionless with respect to its cross-sectionally averaged value, denoted as M_s:

$$M_s = \left[\int_0^h m_s(z)\,\mathrm{d}z \right] / \mathrm{h} \qquad [4]$$

The inflow momentum of both incoming channels is shown in figure 5. Since the momentum is made dimensionless with M_s of the incoming channel, both incoming channels have similar profiles. Notwithstanding their equality in dimensionless form, the total momentum of the tributary is larger than that of the main incoming channel, due to the adopted discharge ratio. The influence of the cross-section can be clearly seen: for the rectangular cross-section, the momentum attains a constant value at a height of about $0.15h$. Under this height, the momentum builds up from zero, as a result of the friction by the rough wall. For the chamfered section and the trapezoidal section, a gradual increase of the momentum can be seen in the regions were inclined walls are present. Since the momentum is relatively lower at the lower heights, the chamfered and especially the trapezoidal section have a relatively higher concentration of momentum closer to the surface.

Off course, the results of figure 5 are attributed to the increasing width in the regions were inclined banks are present. Though this may seem trivial, it nicely shows what the effect is of a change in cross-section on the momentum in a straight channel. The chamfered and trapezoidal section have less momentum at lower depths, while the trapezoidal section has much more momentum near the surface.

4.2   Location of the mixing layer

In this section, the location of the mixing layer is compared for the three numerical simulations. Because the incoming velocity profiles differed clearly in momentum over the vertical, it is expected that this will influence the position of the mixing layer considerably. The mixing layer is localized here by means of the maximum turbulent kinetic energy (TKE) in a certain horizontal plane. In the same way, the shear layer between the separation zone and the contracted section is characterized. Note that, despite of their names (figure 1), the mixing layer and the shear layer in the separation zone both are the manifestations of a shear layer, i.e. a zone where two flows of different velocity meat.

To allow for a comparison of the different cross-sectional shapes, the results are made dimensionless with a length scale equaling the surface width W_d. Hence, the trapezoidal cross-section having a different surface width is rescaled to the dimensions of the rectangular and chamfered section.

Figure 6 presents the mixing layer and the shear layer for all investigated cross-sections, in three horizontal planes: near the surface ($z/h = 1.0$), at mid-depth ($z/h = 0.5$) and at quarter-depth ($z/h = 0.25$) . Each of these heights represents an interesting region regarding the streamwise momentum in the incoming channels (figure 5). At the surface, the momentum of the trapezoidal section is higher, while at $z/h = 0.25$ it is lower than that of the other cross-sectional shapes. At mid-depth, the incoming momentum is approximately equal in all shapes. Regarding the mixing layer, it follows that the trapezoidal section has a mixing layer protruding further to the opposing bank near the surface. At the lowest height however, its mixing layer is located slightly more inward than the mixing layer of the other cross-sectional shapes. The mixing layer of the rectangular and chamfered section are located approximately at the same position, though the rectangular section protrudes somewhat further. Additionally, it can be seen that the mixing layers do not perfectly have the same position in the horizontal planes: they are tilted so that the mixing layers stretch further to the opposite bank near the surface. The mixing layer of the trapezoidal section is exemplary for this behaviour.

Similar phenomena are seen in the shear layer next to the separation zone: the trapezoidal section protrudes differently near the surface than closer to the bottom. However, characterizing the shear layer by means of maximum TKE at $z/h = 0.25$ (figure 6(c)) is difficult due to the changed dimensions of the separation zone in the vertical planes (cf. infra).
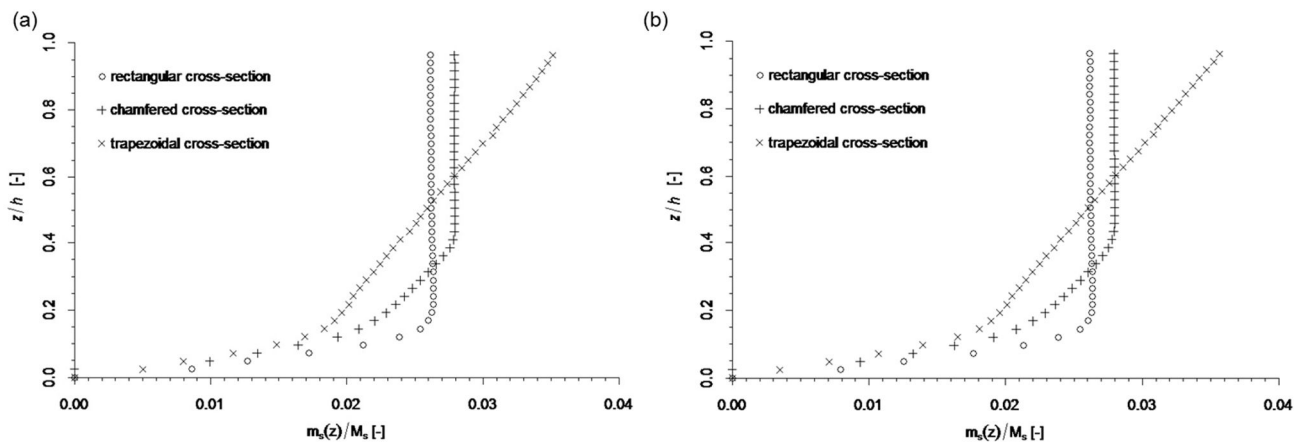

Figure 5. The streamwise momentum averaged over the width $\mathrm{m}_s(z)$ of the different cross-sections in (a) the tributary and (b) the main channel.
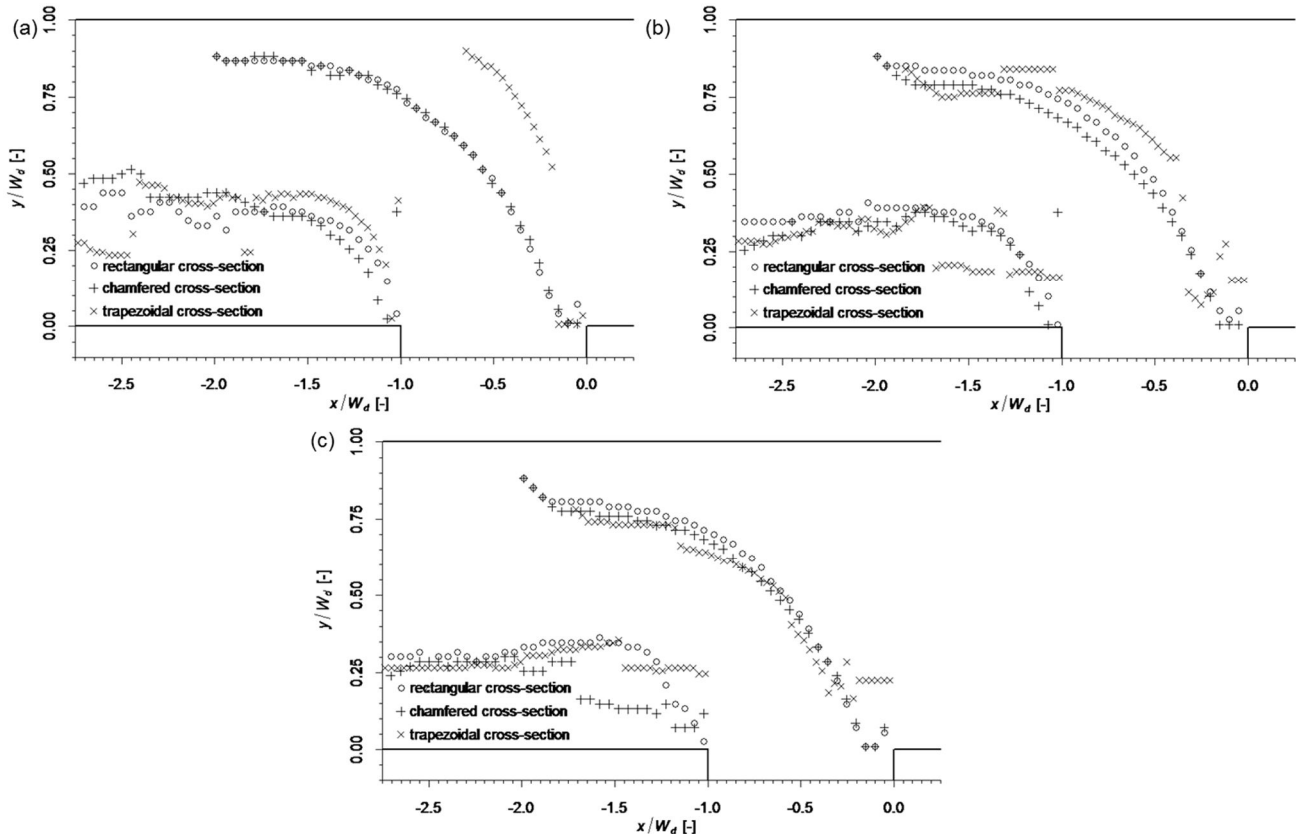
Figure 6. The mixing layer and the shear layer in the separation zone, determined by plotting the maximum TKE,
(a) near the surface ($z/h = 1.0$); (b) at mid-depth ($z/h = 0.5$); (c) at quarter-depth ($z/h = 0.25$).

The shifting location over the vertical of the mixing and shear layer can be explained by the distribution of momentum over the height of the incoming channels. As was demonstrated in figure 5, the trapezoidal section has much higher momentum near the surface, as compared to closer to the bottom. Therefore, the mixing layer near the surface will be pushed further towards the opposing bank. The rectangular section has a quasi-uniform momentum distribution, hence the location of the separation zone will be only marginally different over the height.

4.3 Flow patterns at the surface

In figures 4(b) and 7, the flow velocities near the surface are shown for the different cross-sectional shapes. In these figures, the dotted line represents a zero mean longitudinal velocity ($\bar{u} = 0$), in order to characterize the extent of the separation zone. For comparison purposes, the results of the LSSPIV measurements were presented in figure 4(a). During the validation, a quantitative comparison of experiment and simulation in the chamfered section was already made in figure 3(b), and the agreement was acceptable.

Figure 7(a) can also be compared to the experiments of Shumate (reported in Huang 2000), which were performed in a rectangular section. The comparison is good, as both in the experiment as in the simulation, the line of zero mean longitudinal velocity, $\bar{u} = 0$, extends to about $y/W_d = 0.25$, and reattaches at $x/W_d = -3$. In the experiments, the large downstream velocities in the contracted section start at $y/W_d = 0.5$, which is similar to the values in the numerical simulations.

Between the different cross-sectional shapes, the main difference lies in the extent of the separation zone. For the chamfered section already, it can be seen that the end of the separation zone is not characterized by the contracted flow retaking the complete downstream width, as is the case for the rectangular section. Instead, the separation zone ends due to water surfacing near the left bank. For the trapezoidal section, this behaviour is even more pronounced. It can clearly be seen that there is a three-dimensional effect: flow with a downstream momentum is surfacing relatively shortly after the confluence (at $x/W_d = -1.40$). This flux of longitudinal momentum reduces the velocity difference that drives the shear layer, and as a result the shear layers dissolves more quickly. A close look to a certain width is presented in figure 8. It can clearly be seen that the shear layer has the largest velocity difference and width in the rectangular section. For the chamfered and trapezoidal section, the velocity difference and the width of the shear layer decreases. Hence the downstream velocity is more uniform in the chamfered and trapezoidal section. For the trapezoidal section, it is remarkable that there is no more upstream velocity in this section, as was also noticed in figure 7(b). By looking at some vertical planes in the section 4.4, this phenomenon can be further illustrated.

It should be mentioned that for a given confluence angle, the extent of the separation zone depends on the discharge ratio (Best and Reid, 1984), which was kept at a constant value of $q = 0.25$ in all numerical experiments. For a rectangular section, Best and Reid (1984) offer empirical relations for the dimensions of the separation zone, determined by means of

surface dye tracers. For the discharge ratio of 0.25, these relations predict a maximum width $W_{sep}/W_d = 0.45$ and a length of $L_{sep}/W_d = 2.29$. The predicted maximum width seems to correspond to the present numerical simulations of the rectangular section (figure 7(a)), yet the predicted length differs from the experiments of Shumate and the present simulations.
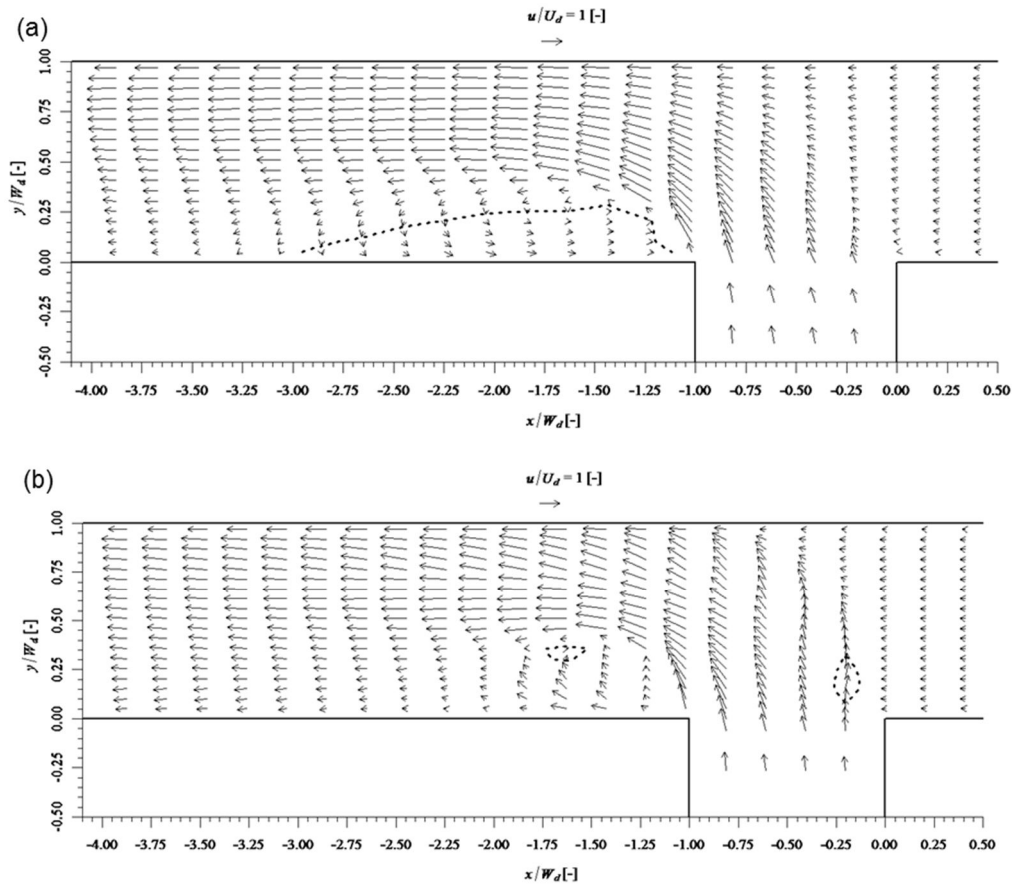

Figure 7. Plot of the simulated velocities near the surface. (a) the rectangular section; (b) the trapezoidal section. The dashed line presents $\bar{u} = 0$.
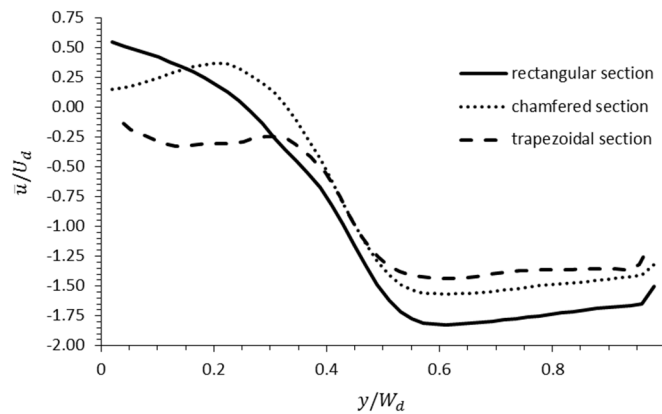

Figure 8. Simulated surface velocity over the width at $x/W_d = -2$.

4.4 Flow patterns in a selection of vertical planes

In this paragraph, flow patterns in a selection of vertical planes are discussed. For model verification purposes, the focus is on the vertical sections that were measured experimentally.

First, the agreement between numerical simulations of the chamfered section with the experiments will be discussed. For the section $x/W_d = -1.33$ (figure 9), the dimensions of the separation zone are quite correctly simulated: the separation zone extends to $y/W_d = 0.25$ and $z/W_d = 0.1$. In the region just below the separation zone, i.e. below $z/W_d = 0.1$, the numerical simulations predict a stronger downstream velocity than measured in the experiments. However, both the experiment and the simulations indicate that this region is not part of the separation zone, i.e. clear downstream velocities are present. In the contracted section, i.e. $y/W_d > 0.35$, where strong downstream velocity prevails, there is a good correspondence on $\bar{u}$, but slightly less on $\bar{v}$. The same goes for section $x/W_d = -2$ (figure 10): the extent of the separation

zone and the longitudinal velocity in the contracted section show an acceptable agreement; only the intrusion of main flow in the separation zone is over-predicted in the numerical simulations.

Secondly, the case of the rectangular section can be compared to experiments reported in literature. The present numerical simulations of the rectangular section actually correspond well to the experiments of Shumate (Huang 2000), notwithstanding the substantial difference in Froude number (in the experiments $Fr = 0.37$ vs. $Fr = 0.05$ in the simulations). In section $x/W_d = -1.33$, there is a steep gradient between the separation zone and a core of strong downstream velocity around $y/W_d = 0.40$. In section $x/W_d = -2$, the extent of the separation zone is correctly modeled, as well as the fact that the intrusion below the separation zone has not reached the left bank. However, the secondary cells in the numerical simulation do not compare well with the experiments, which might be attributed to the difference in Froude number.

In comparison to numerical models applying the Reynolds-Averaged Navier-Stokes equations (Huang 2000, Đorđević 2012), which have been validated against Shumate's experiments, the present LES are better able to predict the curved extent of the separation zone over the vertical.
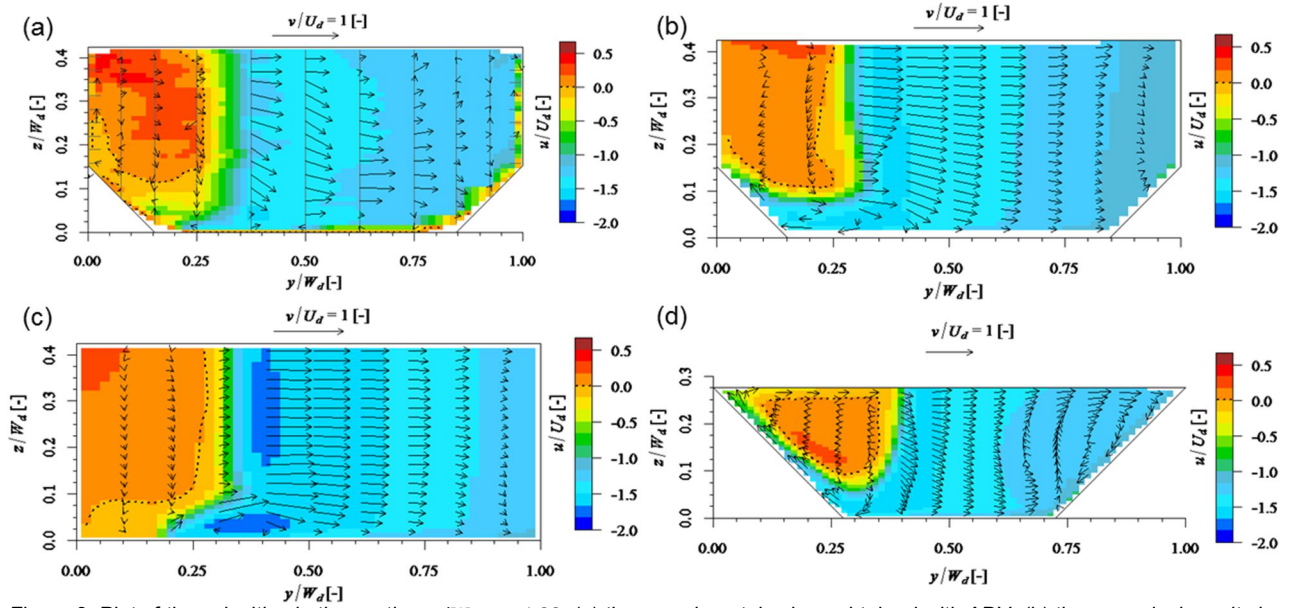

Figure 9. Plot of the velocities in the section $x/W_d = -1.33$. (a) the experimental values obtained with ADV; (b) the numerical results in the chamfered section; (c) the rectangular section; (d) the trapezoidal section. The color scale represents the mean downstream velocity $\bar{u}$, the arrows the mean velocity component in the vertical plane.
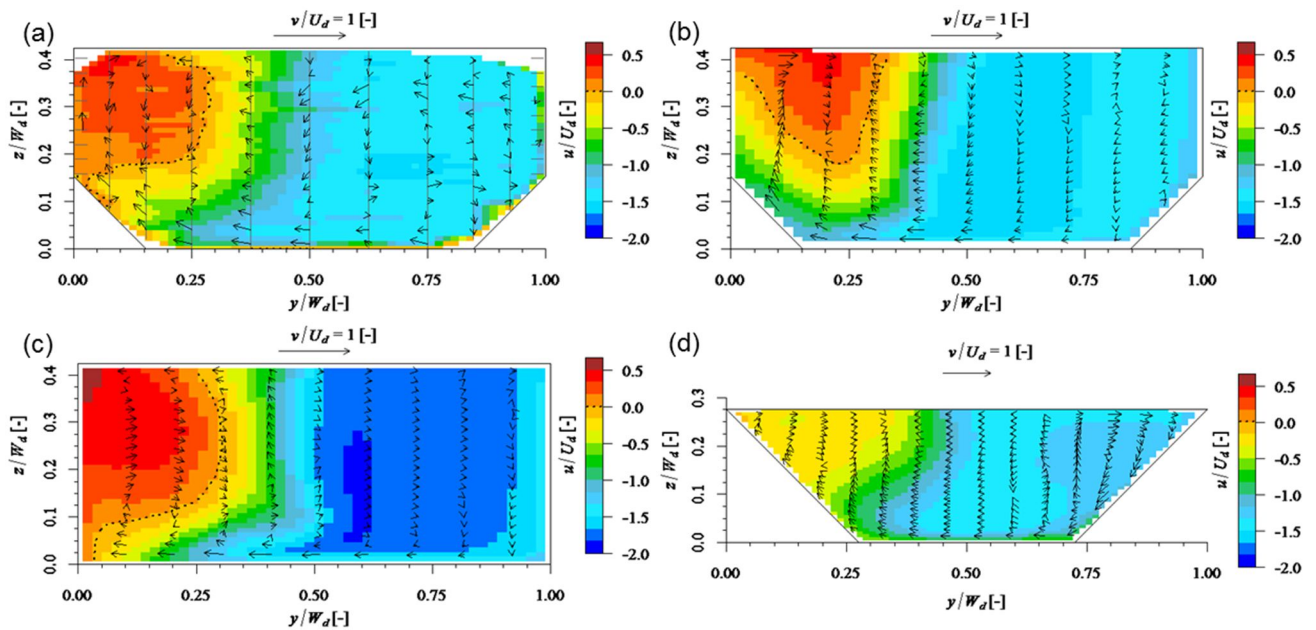

Figure 10. Plot of the velocities in the section $x/W_d = -2$. (a) the experimental values obtained with the ADV; (b) the numerical results in the chamfered section; (c) the rectangular section; (d) the trapezoidal section. The color scale represents the mean downstream velocity $\bar{u}$, the arrows the mean velocity component in the vertical plane.

Comparing the LES predictions for the flow patterns in the rectangular section with the chamfered section, it is noticed how the separation zone of the rectangular section stays more attached to the left bank. In the chamfered section, there is a much larger intrusion of downstream momentum, reducing the size of the separation zone. Since this intrusion of downstream velocity follows the wall boundaries for all cross-sections, it seems like the chamfers aid the vertical transfer of downstream momentum. Regarding the trapezoidal section, similar conclusions can be drawn. Here, the intrusion of downstream momentum is more pronounced than for the chamfered section, leading to a separation zone that quickly detaches from the left bank (figure 9(d)). In the more downstream section (figure 10(d)), there is no more upstream velocity present. Hence, it is again concluded that the downstream velocity is more uniformly distributed in the section, i.e. the trapezoidal section enhances the mixing process.

The intrusion of downstream momentum via the left bank that was seen in the vertical planes, helps to understand what was seen in the surface flow patterns before, namely surfacing flow near the left bank.

The origin of the stronger intrusion of downstream momentum in the chamfered and trapezoidal sections is finally discussed by examining vertical planes in the confluence area itself. Figure 11 presents vertical planes in the main channel taken at a position halfway of the inclined left bank of the tributary channel, as indicated on figure 11(a). The goal is to investigate why the chamfered and trapezoidal section exhibit a zone of intrusion below the separation zone. In the rectangular section, where no inclined bank is present, the transverse inflow from the tributary section is rather uniform. Close to the bottom, a region of stronger downstream velocity develops, resulting in the flow patterns seen downstream (figure 9(c)). For the chamfered and trapezoidal section, it can be seen that at the lee side of the inclined bank, a zone of strong downstream velocity is present. This zone is present over the whole width of the tributary channel, and originates at the stagnation zone in the upstream corner of the confluence. The reduced streamwise momentum that is present near the bottom of the chamfered and trapezoidal sections (recall figure 5) might enhance the formation of this zone, in contrast to the rectangular section. Additionally, a secondary circulation originates at the lee side of the inclined bank (figure 11), which is attributed to the bank inclination working as a kind of "backward facing step". This secondary circulation will lead to the increased intrusion of streamwise momentum in sections further downstream. In figure 11, it can already be seen that the secondary circulation is stronger for the trapezoidal section, which explains the shorter lifespan of its recirculation zone.
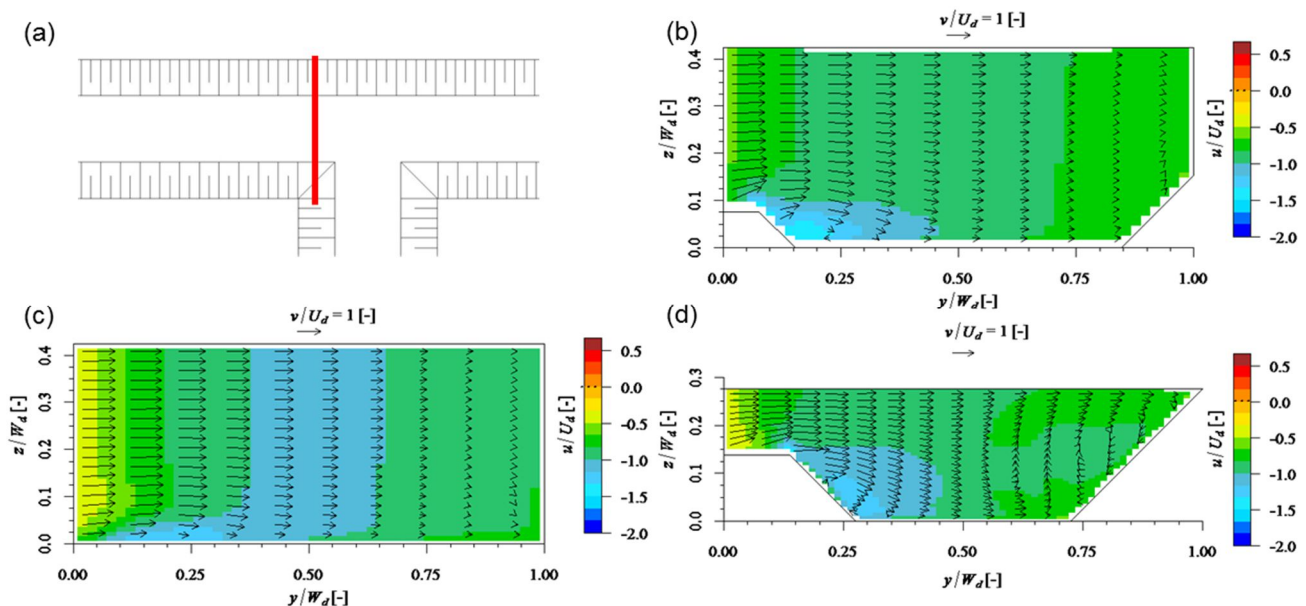

Figure 11. Plot of the velocities at the section indicated in (a). Figure (b) presents the numerical results in the chamfered section; (c) the rectangular section; (d) the trapezoidal section. The color scale represents the mean downstream velocity $\bar{u}$, the arrows the mean velocity component in the vertical plane.

5. CONCLUSIONS

The research question addressed in this paper, was to which extent the experimental knowledge acquired in schematized open channel confluences with rectangular cross-sections still holds in case of non-rectangular shaped cross-sections. To that end, large-eddy simulations (LES) were applied to investigate the effect of cross-sectional shape on the flow patterns in a confluence. Three cross-sectional shapes typical for man-made canals were studied: a rectangular, a chamfered rectangular and a trapezoidal section. The LES were validated against laboratory measurements in a confluence with a chamfered cross-section and were additionally compared to experiments reported in literature for a confluence with a rectangular section. The simulations, which resolve the time-dependent flow structures, were found to agree acceptably well with the experiments.

It was found that the locations of the mixing layer between the incoming flows and the shear layer between the separation zone and the contracted section (see figure 1 for the case with rectangular sections), protrude further towards the

opposing bank in case of the trapezoidal section, at least near the surface. Closer to the bottom, however, the mixing layer protrudes less far. The observed differences can be linked with the incoming momentum distribution over the height.

Surface velocity and vertical sections also showed that the separation zone evolves differently. When inclined banks are present, downstream momentum intrudes much faster in the separation zone, leading to a faster break-up of the separation zone. This effectively decreases the velocity difference over the shear layer, and leads to a faster uniformisation, especially for trapezoidal sections. It was found that the downstream corner of the confluence plays a major role in the aforementioned evolution of the separation zone.

Referring to the research question, the well-known flow patterns in rectangular sections (figure 1) are obviously still present in other cross-sectional shapes. Yet, inclined banks result in the aforementioned differences for the shear layers and the separation zone. In a trapezoidal section, it might be difficult to define the dimensions of the separation zone in a similar way as has been done in rectangular sections (see e.g. Best and Reid 1984).

For field studies on confluences, the current research pointed out the importance of characterizing the bathymetry of corners and the incoming momentum distribution. As a non-uniform momentum distribution leads to a different location of the mixing layer, it is worth measuring this boundary condition accurately.

The outcome of the present numerical simulations may be interpreted as a call for extra experiments under controlled conditions in non-rectangular sections, as these might further contribute to the knowledge on confluence hydrodynamics. Finally, it should be mentioned that in this paper only one discharge ratio was considered, a parameter setting which certainly should be assessed in further research.

ACKNOWLEDGMENTS

REFERENCES

Anwar H. 1955. *Strömungsverhältnisse bei Flußvereinigungen*. PhD dissertation TH Karlsruhe, 64 pp.

Best J. and Reid I. (1984). Separation zone at open-channel junctions. *Journal of Hydraulic Engineering,* 110, 1558-1594.

Blanckaert K., Duarte A. and Schleiss A.J. (2010). Influence of shallowness, bank inclination and bank roughness on the variability of flow patterns and boundary shear stress due to secondary currents in straight open-channels. *Advances in Water Resources*, 33, 1062-1074.

Creëlle S., De Mulder T., Schindfessel L. and Van Oyen T. (2014). Influence of hydraulic resistance on flow features in an open channel confluence. 3rd IAHR Europe Congress, Ed. de Almeida et al., Porto, 10 pp.

Constantinescu G., Miyawaki S., Rhoads B. and Sukhodolov A. (2012). Numerical analysis of the effect of momentum ratio on the dynamics and sediment-entrainment capacity of coherent structures at a stream confluence. *Journal of Geophysical Research*, 117, 21 pp.

Coussement A., Gisquel O. and Degrez G. (2012). Large eddy simulation of a pulsed jet in cross-flow. Journal of Fluid Mechanics, 695, 1-34.

Đorđević D. (2012). Application of 3D numerical models in confluence hydrodynamics modeling. IXI International Conference on Water Resources, Urbana-Champaign, 8 pp.

Goring G. and Nikora V. (2002). Despiking acoustic Doppler velocimetry data. *Journal of Hydraulic Engineering*, 128 (10), 117-126.

Huang J. (2000) *Development and validation of a three-dimensional numerical model for application to river flow*. PhD dissertation University of Iowa, 122 pp.

Khublaryan M. (2009) Surface waters: rivers, streams, lakes and wetlands. *Types and properties of water*. Ed. M. Khublaryan, Oxford, 16 pp.

Nezu I., Nakagawa H. and Rodi W. (1989). Significant difference between secondary currents in closed channels and narrow open channels. *23rd IAHR Congress*, Ed. T. Dick and J. Ploeg, Ottawa, 125-133.

Rice S., Roy, A. and Rhoads B. (2008). *River confluences, tributaries and the fluvial network*. Wiley & Sons, 456 pp.

Rodi W., Constantinescu G. and Stoesser T. (2013). *Large-eddy simulations in hydraulics*. CRC Press/Balkema, 251 pp.

Sagaut P. (2006). *Large eddy simulation for incompressible flows*. Springer, 558 pp.

Schindfessel L., Creëlle C., Boelens T. and De Mulder T. (2014). Flow patterns in an open channel confluence with a small ratio of main channel to tributary discharge. *River Flow 2014*, Eds. A.J. Schleiss et al., Taylor & Francis Group, London.

Stoesser T. (2014). Large-eddy simulation in hydraulics: Quo vadis? *Journal of Hydraulic Research*, 52 (4), 441-452.

Tominaga A., Nezu I., Ezaki H. and Nakagawa H. (1989). Three-dimensional turbulent structure in straight open channel flows. *Journal of Hydraulic Research*, 27 (1), 149-173.

van Balen W., Uijttewaal W. and Blanckaert K. (2009). Large-eddy simulation of a mildly curved open-channel flow. *Journal of Fluid Mechanics*, 630, 413-442.

Wahl T. (2003). Discussion of "Despiking acoustic Doppler velocimetry data". *Journal of Hydraulic Engineering*, 129 (6), 484-487.